Viscoelastic and High Strain Rate Response of Anisotropic Graphene-Polymer Nanocomposites Fabricated with 3D Stereolithography Printing

Chang Quan Lai[1,*], Kalaimani Markandan[1], Boyang Luo[1], Yee Cheong Lam[2], Wai Chun Chung[3], & Arunraj Chidambaram[4]

[1]*Temasek Laboratories, Nanyang Technological University, 50 Nanyang Drive, Singapore 637553*

[2]*School of Mechanical & Aerospace Engineering, Nanyang Technological University, 50 NanyangAvenue, Singapore 639798*

[3]*School of Physical & Mathematical Sciences, Nanyang Technological University, 21 Nanyang Link, Singapore 637371*

[4]*School of Materials Science & Engineering, Nanyang Technological University, 50 Nanyang Avenue, Singapore 639798*

[*]cqlai@ntu.edu.sg

Keywords: Graphene Nanocomposite, 3D Printing, Viscoelastic, High Strain Rate, Aligned Graphene

Abstract

The viscoelastic and high strain rate response of stereolithographically 3D printed graphene - PMMA nanocomposites was investigated using dynamic mechanical analysis (DMA) and the Split-Hopkinson pressure bar. The obtained experimental data were compared with the quantitative predictions of a simple viscoelastic micromechanical model. Our results confirmed that property anisotropy of the graphene nanocomposites arose from the alignment of graphene platelets along the

printing axis within the polymer matrix. If a load is applied along this axis, the nanocomposite will adopt an isostrain (Voigt) geometry, exhibiting large dynamic modulus and strength values. These properties were found to improve with increasing graphene concentrations, up to 0.05 wt. %, and post-print bake temperatures, up to 120 °C. Supporting evidence from differential scanning calorimetry and DMA temperature sweep test indicates that this is due to good interfacial bonding between the graphene and polymer, which allowed for efficient load transfer, and that a post-print heat treatment can increase the degree of cure in the polymer. Similar trends were observed for complex lattices fabricated using the same method. Comparing the dynamic mechanical properties of the graphene nanocomposites against that of other lightweight engineering materials, it was found that the nanocomposites exhibited specific strengths that were higher than most Al alloys and comparable to the best literature values reported for graphene – polymer and carbon nanotube – polymer composites. The additively manufactured graphene nanocomposite lattices also showed better energy absorption capabilities than syntactic ceramic foams and Al foams on a per unit weight basis. These results are remarkable considering that the amount of graphene added ($\leq$ 0.10 wt.%) was an order of magnitude lower than that usually employed in other studies.

1. Introduction

Graphene is a 2D material with exceptional physical[1,2], mechanical[3], thermal[4], optical[5], electrical [6,7] and chemical properties [8]. When incorporated into polymers to form a composite, it can be used as a strain sensor [9], electromagnetic interference shield [10], organic solar cells [11,12] and cancer therapy [13,14]. One of the most promising applications of graphene-polymer composites is in the field of structural materials, as significant enhancement in the mechanical properties of various polymers have consistently been observed, even at low graphene concentrations [15–17]. To improve the ease of dispersion and interfacial bonding with polymers, graphene oxide is often used in place of graphene [18–20]. However, the same oxygen-containing moieties that promote interactions with solvents and polymer also disrupt the sp^2 bonding in graphene, degrading its mechanical properties [21]. For instance, it has been experimentally determined that the Young's modulus of monolayer graphene oxide is only one-fifth that of monolayer graphene (~ 200 GPa vs ~ 1 TPa) [3,22].

There are multiple methods of dispersing graphene in polymers, such as solution blending [23], mechanical mixing [15], in situ polymerization [17] and melt mixing [24]. In terms of shape formation, however, the majority of studies continue to rely on casting, which involves the infusion of graphene-polymer mixtures into a mould for solidification. While casting is generally a straightforward and simple process, it can face serious limitations in generating complex 3D structures due to mould filling and mould release considerations. Because of this, there has been a movement towards the use of 3D printing for the production of graphene-polymer composites in recent years [25]. These 3D printing techniques typically involve the extrusion of heated graphene-polymer composite filaments (*e.g.* fused deposition modeling) [26,27] or photopolymerization of graphene-polymer resins in spatially selective areas (*e.g.* digital light printing, stereolithography) [15,18,28]. By successively depositing these layers of materials, a complex 3D geometry can then be produced in its net shape without any mould.

While extrusion-based techniques have the advantage of being simpler and cheaper to operate, photopolymerization-based 3D printing can offer better printing speeds, improved resolution and smooth surfaces that are comparable to injection moulded parts. The main challenge, however, is to ensure that sufficient light reaches the polymer resin for polymerization during 3D printing, as graphene has a strong tendency to absorb light at the wavelength commonly used for photopolymerization (~ 405 nm) [29]. As a result, the polymer matrix of graphene composites fabricated this way are usually under-polymerized, and the stiffness and strength of the graphene composites would be lower than that of the unadulterated polymer [18,28–30]. To rectify this, a post-print curing step utilizing light and/ or heat is required, after which the mechanical properties of the composite will rebound, often exceeding those of the neat polymer [15,18,30].

Although graphene's strong absorbance of the photopolymerizing light can be a hindrance to the 3D printing process, it does confer one unique advantage. A recent study has found that this property can lead to the alignment of graphene platelets along the print axis through a proposed Self-selection of Naturally Aligned Graphene (SNAG) process [15] (Fig. 1). Essentially, because graphene can reduce the transmission of laser light by more than half at a wavelength of 405 nm (the wavelength used in most stereolithography 3D printers) [29], the platelets can create a shadow effect, preventing sufficient laser light from reaching the photosensitive resin behind them for polymerization and solidification of the liquid resin. Horizontally oriented platelets are more effective in blocking the laser light and preventing polymerization than vertically oriented platelets due to graphene's unique 2D morphology *i.e.* large area, small thickness (Fig. 1, middle). Therefore, whenever the build plate detaches a polymerized layer from the resin tank, the vertically aligned graphene, with its solidified, polymerized surroundings, would be securely incorporated into the print layer while the horizontal platelets, surrounded with liquid, unpolymerized resin due to the shadow effect, would not (Figure 1, right). As a result, only graphene platelets aligned to the print axis would be present in the final print. This alignment of graphene platelets allows the composite to adopt an isostrain (Voigt) arrangement

that sharply enhances the stiffness and strength of the polymer, even at extremely low graphene concentrations. While there are other methods of producing aligned graphene composites, such as freeze casting [31], vacuum filtration [33] and employing strong magnetic fields [32,33], the SNAG process is simpler, in that it does not require extreme changes to the environmental conditions, special materials or a mould for producing aligned graphene in complex geometries.

Despite the wealth of research in graphene-polymer composites, however, the dynamic mechanical behaviour of these materials has not been characterized as extensively as their quasistatic counterpart [20,34,35]. Information on this dynamic performance, which can be vastly different from that under static loading due to the viscoelastic nature of polymers, is important for engineering against flow-induced structural instability (*i.e.* fluttering) in aircraft wings [36], low frequency vibrations on tennis rackets that contribute to player fatigue [37] and shock loadings in crumple zones of cars [38], as well as golf clubs [39]. Without such studies, it would be difficult to apply these graphene-polymer composites to aerospace components, automobile parts and high-performance sports equipment, where their lightweight, stiff and strong characteristics can be exploited.

For this reason, in the present study, we aim to characterize the dynamic behaviour of the aforementioned aligned-graphene/ PMMA nanocomposite fabricated using stereolithographic 3D printing [15]. This material had been found to give the greatest enhancement in quasistatic mechanical properties per unit weight of graphene added, but it remains unclear if this remains true under dynamic loading. A dynamic mechanical analyzer (DMA) will be used to measure the graphene nanocomposite's dynamic modulus at low frequencies ($\leq$ 100Hz), which is the relevant range for fluttering and long range structural vibrations, while its strength at high strain rates (~ 1000 /s) will be characterized using the Split-Hopkinson pressure bar. A simple quantitative model will also be derived to estimate the viscoelastic and high strain rate response of the graphene-PMMA nanocomposite, and finally, its performance will be compared against that of other lightweight structural materials.

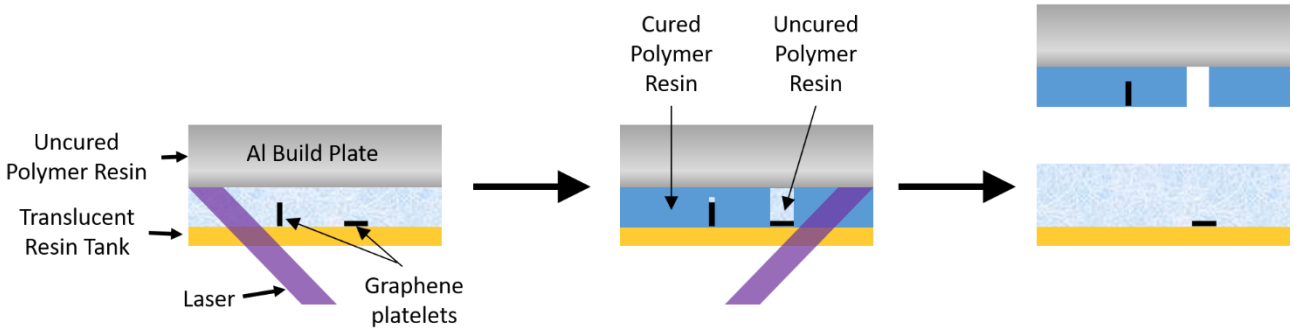

Figure 1: Schematic diagram illustrating the Self-selection of Naturally Aligned Graphene (SNAG) process *[15]*. **As the laser sweeps across the polymer resin (left), horizontal graphene platelets block the laser light, preventing polymerization of the photosensitive resin above them (middle). This effect is much less pronounced if the platelets are vertically oriented, due to the small thickness of graphene. Therefore, only the vertical platelets would be incorporated into the polymerized layer when the Al build plate rises to detach the layer from the resin tank (right).**

2. Materials and Methods

2.1 Graphene-Polymer Mixture

Graphene platelets (Graphene Industries Ltd, U.K.) with a nominal size of 15–25 µm were added to Grey Resin (Formlabs Inc., USA), which is Formlabs' commercial name for a photosensitive liquid mixture of methacrylate oligomers and monomers. Raman spectroscopy results reported previously showed that the graphene platelets consist mainly of few-layer (~ 5 layers) graphene and polymerized Grey Resin is largely polymethyl methacrylate (PMMA) [15]. The graphene concentration was varied from 0.02 wt. % to 0.10 wt. %, beyond which no structure could be reliably 3D printed. 200ml of the mixture was mechanically stirred in a borosilicate glass beaker, using a Teflon coated magnetic stirrer, for 45 min at a setting of 1500 rpm, followed by 20 min of ultrasonication at 37 kHz (Elmasonic S 30 H, Germany).

2.2 3D Printing

The graphene/Grey Resin mixture was transferred to a commercial stereolithography 3D printer, Form 2 (Formlabs Inc, USA), which uses a laser (wavelength = 405 nm) to polymerize the mixture according to the input of a STL file. Neat Grey Resin samples, without any addition of graphene, were fabricated as well to act as controls. The STL file was generated using Solidworks (Dassault Systemes SE, France). Cuboid-shaped samples (30 mm x 12 mm x 4 mm) were 3D printed for DMA tests while cylindrical samples (diameter = 9 mm, height = 3 mm) were fabricated for Split-Hopkinson pressure bar tests (Fig. 2). The printing direction was varied for the cuboids but fixed for the cylinders, normal to the circular surface. The layer resolution was 0.05 mm for all samples and the density of the printed material was 1.20 g/cm^3; the addition of small amounts of graphene did not change the density of the polymer appreciably. After printing, the samples were immersed in isopropyl alcohol (IPA) for 5 minutes to remove excess liquid resin. Raman spectroscopy had previously shown that the 3D printing process did not change the characteristics of the graphene nanoplatelets [15].

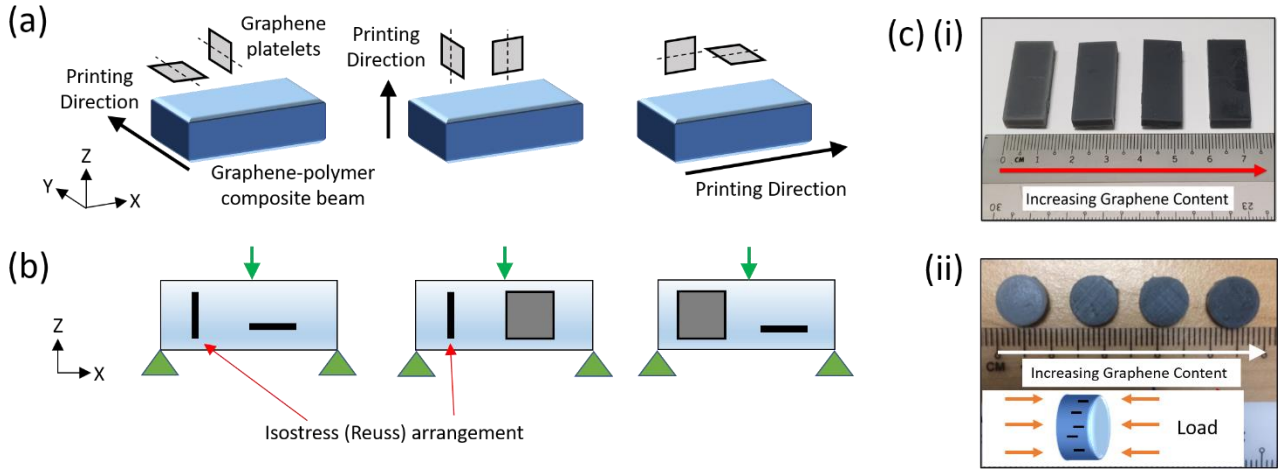

Figure 2: (a) Schematic diagrams illustrating the different print directions for the cuboid samples and the possible orientations of the graphene platelets due to the SNAG process. (b) Schematic diagrams illustrating the possible orientations of the graphene platelets in the cuboid

samples when loaded in the 3-point bending arrangement for DMA testing. The orientations that result in an isostress (Reuss) configuration are indicated. The rest of the orientations would result in an isostrain (Voigt) stress distribution. (c) Photographs of the (i) cuboid samples for DMA testing (ii) cylindrical samples for high strain rate testing. (Inset) A schematic diagram illustrating the orientation of the graphene platelets with respect to the direction of the impact load applied (orange arrows).

2.3 Heat Treatment

After 3D printing and cleaning, the polymer-graphene samples were placed in an oven (Memmert Universal, Schwabach, Germany) for further curing at 80 °C, 120 °C and 160 °C for a duration of 60 min. The oven was preheated to the desired temperature before the samples were inserted. The heat treatment did not have any appreciable effects on the graphene nanoplatelets [15].

2.4 Scanning Electron Microscopy

Scanning electron microscopy (SEM) was performed using JSM-7600F (JEOL Inc., Japan) with an accelerating voltage of 2-5 kV. To improve the imaging resolution, 5 nm of platinum was deposited onto the samples' surfaces using a Polaron sputter coater.

2.5 Differential Scanning Calorimetry

Differential scanning calorimetry (DSC) analysis was carried out on the samples using DSC 2010 (TA Instruments, USA), at a scanning rate of 10 °C/min from -10 °C to 200 °C in nitrogen atmosphere.

2.6 Dynamic Mechanical Analysis

The dynamic mechanical analysis (DMA) was performed on the cuboid samples using DMA Q800 (TA Instruments, USA) with the 3-point bending clamp. For the frequency sweep operation (1 – 100 Hz) under isothermal condition (27 °C), a preload force of 0.01 N and an amplitude of 15 µm were used. For the temperature sweep operation, the frequency was fixed at 1 Hz and the amplitude at 15 µm, as the temperature was varied from 30 °C to 150 °C at a ramp rate of 3 °C/min. It has been verified that at such small displacements, the viscoelastic response of the material is independent of the strain amplitude. Thus, such settings are suitable for measuring the linear viscoelastic properties of the material (Fig. 3a and 3b).

2.7 Low Strain Rate Compression Test

Low strain rate compression test of cylindrical samples (height = 3 mm, diameter = 9mm) was carried out using Shimadzu Autograph AG-500A (Shimadzu Corporation, Kyoto, Japan) with a 50 kN load cell at a strain rate of ~ 1 /s. The engineering stress-strain curve can be calculated from the force (N) and displacement (mm) measurements recorded by a data acquisition software (Trapezium, Shimadzu Corporation, Kyoto, Japan) during the test.

2.8 High Strain Rate Compression Testing

High strain rate uniaxial compression testing (~ 1000 /s) of cylindrical samples (height = 3 mm, diameter = 9mm) was conducted using the conventional Split-Hopkinson pressure bar (SHPB) apparatus [20,34,35] (Fig. 3c). At least 2 separate samples were tested and averaged for each data point. The SHPB comprises mainly of the striker bar, incident bar and transmitted bar, which were all made of the same aluminium (Al) 7075-T6 material with a Young's modulus of 71.7 GPa. The diameter of the three bars was 20 mm and the length of the incident bar was 1.17 m. The faces of the

3D printed cylindrical samples were thinly lubricated, to minimize frictional effects, and then placed between the incident and transmitted bars.

The experiment began when the striker bar, powered by compressed gas, impacted the incident bar. The stress wave travelled through the incident bar to the sample and split into the reflected and transmitted stress waves. Measurements of the incident and reflected stress waves were performed via a strain gauge mounted on the incident bar, while the transmitted stress wave was recorded by a strain gauge mounted on the transmitted bar. Entering these measurements into established equations derived from the 1D stress wave theory allowed the sample's dynamic stress-strain curve to be computed [20,34,35].

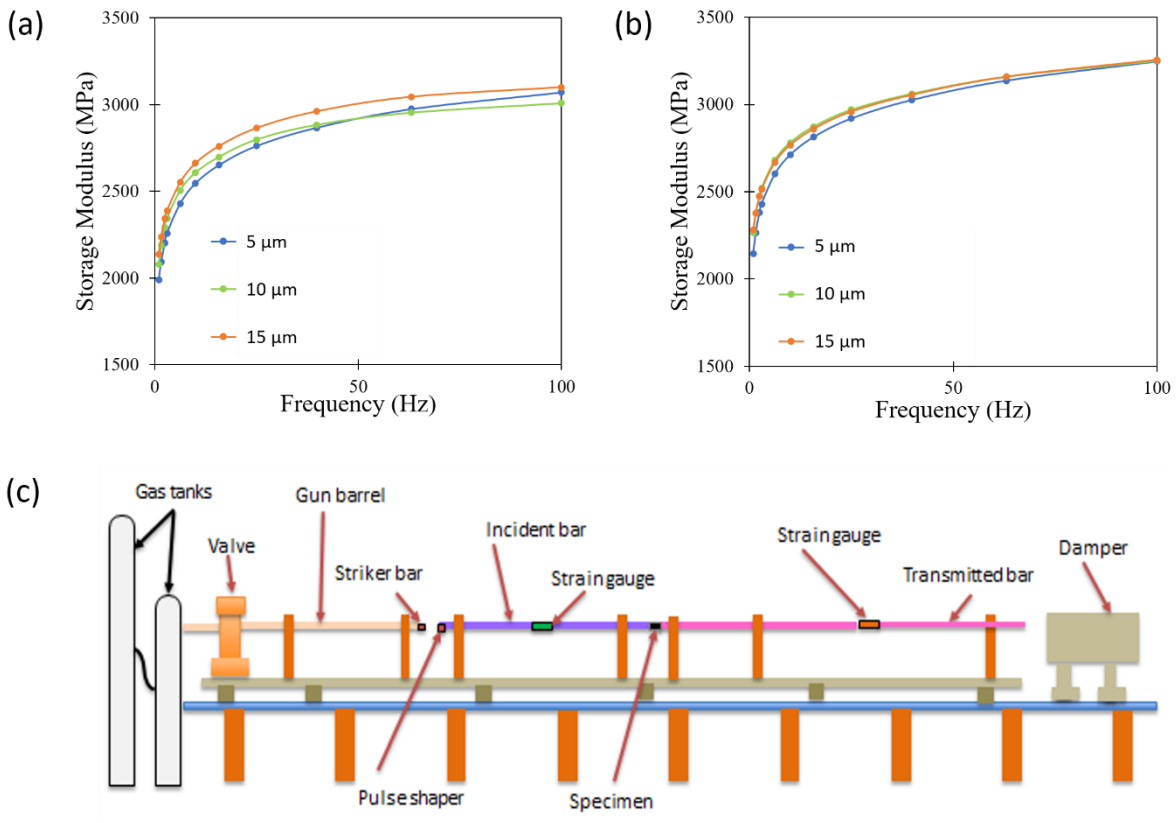

Figure 3: Experimental measurements of the storage modulus of samples containing (a) 0 wt. % and (b) 0.02 wt. % graphene for the displacement amplitudes of 5 µm, 10 µm and 15 µm. The print axis was parallel to the length of the cuboid samples. The samples were cured at 120 °C for

60 min before the DMA tests. (c) Schematic illustration of the Split-Hopkinson pressure bar setup.

3. Micromechanical Modelling

3.1 Dynamic Modulus of Polymer

As a first order approximation, it shall be assumed that the neat polymer follows the viscoelastic response of a Maxwell material. Advanced models such as the Halpin-Tsai equations and the standard linear model were not employed as they can be too detailed and involve many parameters that can unnecessarily complicate the analysis here, thereby obscuring some of the simpler physical insights and relations that we aim to derive from the results. The basic Kelvin-Voigt material model was also not used because it would have yielded a frequency-independent storage modulus, which was found to be incompatible with the results to be presented later.

Based on the Maxwell model presented in Fig. 4a, the constitutive equations can be written as

$$\sigma_{eff} = \sigma_{pS} = \sigma_{pD} \tag{1}$$

and

$$\varepsilon_{eff} = \varepsilon_{pS} + \varepsilon_{pD} \tag{2}$$

where

$$\sigma_{pS} = E_p \varepsilon_{pS} \tag{3}$$

and

$$\sigma_{pD} = \eta_p \dot{\varepsilon}_{pD} = \eta_p \frac{d\varepsilon_{pD}}{dt} \tag{4}$$

σ refers to stress, ε refers to strain, E refers to the Young's modulus and η refers to the viscosity of the material. $\dot{\varepsilon}$ in Eq. (4) refers to the time derivative of strain. The subscripts, "*pS*" and "*pD*", refer to "polymer spring" and "polymer dashpot" respectively, while "*eff*" refers to "effective", that is, the overall stress or strain of the material. Combining Eq. (1) – (4) leads to

$$\dot{\varepsilon}_{eff} = \frac{\dot{\sigma}_{eff}}{E_p} + \frac{\sigma_{eff}}{\eta_p} \tag{5}$$

In the dynamic mechanical analysis (DMA) test, the stress and strain of the material varies in a sinusoidal wave. In other words,

$$\sigma_{eff} = \sigma_0 e^{i\omega t} \tag{6}$$

and

$$\varepsilon_{eff} = \varepsilon_0 e^{i\omega t} \tag{7}$$

Substituting Eq. (6) and (7) into Eq. (5), the complex modulus, E^*, of the Maxwell material can be derived as

$$E^* = \frac{\sigma_0}{\varepsilon_0} = \frac{\eta^2\omega^2 E_p}{{E_p}^2+\eta^2\omega^2} + i\frac{\eta\omega {E_p}^2}{{E_p}^2+\eta^2\omega^2} \tag{8}$$

$$E' = \frac{\eta^2 E_p \omega^2}{{E_p}^2+\eta^2\omega^2} \tag{9}$$

$$E'' = \frac{\eta {E_p}^2 \omega}{{E_p}^2+\eta^2\omega^2} \tag{10}$$

The real part of the complex modulus (Eq. 8) is the storage modulus, E' (Eq. 9), and the imaginary part is the loss modulus, E'' (Eq. 10).

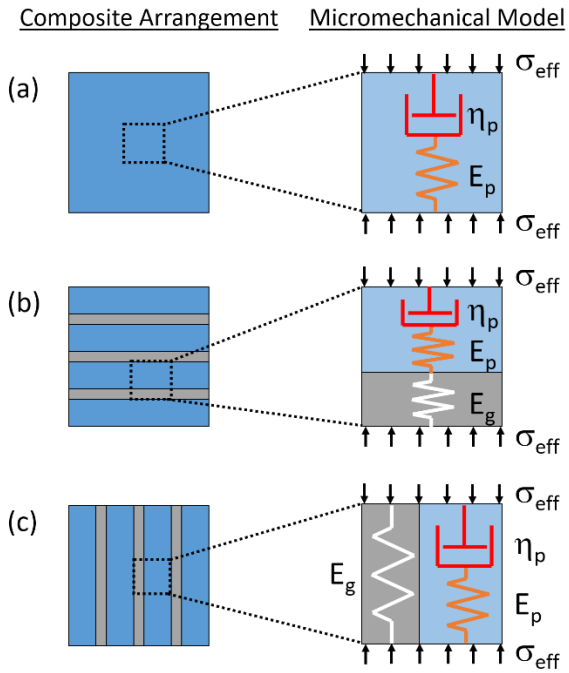

Figure 4: Schematic diagrams showing the equivalent micromechanical arrangement of springs and dashpots for (a) neat PMMA (a.k.a. Grey Resin) (b) isostress (Reuss) arrangement of graphene-PMMA nanocomposite (c) isostrain (Voigt) arrangement of the graphene-PMMA nanocomposite. σ refers to stress, *E* refers to the Young's modulus and η refers to the viscosity of the material. The subscripts, "*p*", "*g*" and "*eff*", refer to "polymer", "graphene" and "effective" respectively.

3.2 Dynamic Modulus of Graphene-Polymer Nanocomposite

Next, we consider the upper and lower bounds of the graphene-PMMA nanocomposite's modulus. They correspond to the isostrain and isostress arrangement respectively. For the isostress configuration (Fig. 4b), *i.e.* Reuss composite, both the graphene platelets and the polymer matrix experience the same stress; thus, its constitutive relationships can be expressed as

$$\sigma_{eff} = E_g \varepsilon_g = E_p \varepsilon_{ps} = \eta \dot{\varepsilon}_{pD} \tag{11}$$

$$\dot{\varepsilon}_{eff} = \frac{\dot{\sigma}_{eff}}{E_g} f_g + \frac{\dot{\sigma}_{eff}}{E_p} f_p + \frac{\sigma_{eff}}{\eta_p} f_p \tag{12}$$

The subscript "*g*" refers to "graphene". The atomic structure of graphene does not support a viscous response, unlike polymers that consist of molecular chains that can slip past each other. Thus, it is appropriate to assume here that graphene undergoes a time-independent elastic response (*i.e.* no viscous component). A recent study appears to indicate that graphene oxide may exhibit a viscoelastic response, but even then, the viscous component was minimal (tan $\delta \sim 0.01$) [41]. f_g and f_p refer to the volume fraction of the graphene and polymer present in the composite respectively. Note that

$$f_g + f_p = 1 \tag{13}$$

Substituting Eq. (3), (4), (6) and (7) into Eq. (11) and (12) will then give the storage and loss moduli of the isostress composite as

$$E' = \frac{\left(\frac{f_g}{E_g}+\frac{f_p}{E_p}\right)\omega^2}{\left(\frac{f_p}{\eta_p}\right)^2+\left(\frac{f_g}{E_g}+\frac{f_p}{E_p}\right)^2\omega^2} \tag{14}$$

$$E'' = \frac{\frac{f_p}{\eta_p}\omega}{\left(\frac{f_p}{\eta_p}\right)^2+\left(\frac{f_g}{E_g}+\frac{f_p}{E_p}\right)^2\omega^2} \tag{15}$$

It can be observed from Eq. (14) and (15) that in the absence of the viscous component of the polymer (*i.e.* $\eta_p \rightarrow \infty$), the complex modulus would reduce to

$$E^* = \frac{1}{\frac{f_g}{E_g}+\frac{f_p}{E_p}} \quad , \tag{16}$$

which is the exact expression for the effective modulus of a composite consisting of 2 elastic solids arranged in an isostress configuration [41].

For the isostrain geometry, both the graphene and polymer would be subjected to the same strain and thus, the constitutive equations are

$$\sigma_{eff} = f_g\sigma_g + f_p\sigma_{pS} \tag{17}$$

$$\sigma_{pS} = \sigma_{pD} \tag{18}$$

$$\sigma_{eff} = \varepsilon_g = \frac{\sigma_g}{E_g} \tag{19}$$

$$\dot{\varepsilon}_{eff} = \frac{\dot{\sigma}_{pS}}{E_p} + \frac{\sigma_{pD}}{\eta_p} \tag{20}$$

which lead to

$$E' = \frac{f_g E_g \left(\frac{E_p}{\eta_p}\right)^2 + (f_g E_g + f_p E_p)\omega^2}{\left(\frac{E_p}{\eta_p}\right)^2 + \omega^2} \tag{21}$$

$$E'' = \frac{f_p \frac{{E_p}^2}{\eta_p}\omega}{\left(\frac{E_p}{\eta_p}\right)^2 + \omega^2} \tag{22}$$

Again, if the viscous component of the polymer does not exist (*i.e.* $\eta_p \rightarrow \infty$), the complex modulus would be

$$E^* = f_g E_g + f_p E_p \quad , \tag{23}$$

which is equivalent to the modulus for 2 perfectly elastic solids arranged in an isostrain configuration [41].

3.3 Dynamic Strength of Graphene-Polymer Nanocomposite

Focusing on the isostrain geometry, since the SPHB test samples were fabricated and loaded in that way (Fig. 2cii), we can rearrange Eq. (17) into

$$\sigma_g = \frac{\sigma_{eff}}{f_g + f_p \frac{E_p}{E_g}} \tag{24}$$

Also, the isostrain geometry, by its definition implies that

$$\frac{\sigma_p}{E_p} = \frac{\sigma_g}{E_g} \tag{25}$$

Substituting Eq. (24) into Eq. (25) yields

$$\sigma_{eff} = \sigma_p \left(f_g \frac{E_g}{E_p} + f_p \right) \tag{26}$$

If it is assumed that the peak stress achievable by the composite is limited by the strength of the polymer, then failure of the composite occurs when $\sigma_p \geq \sigma_{pf}$, where σ_{pf} refers to the failure strength of the neat polymer. Replacing σ_p with σ_{pf} in Eq. (26) would then yield the theoretical peak stress of the composite.

4. Results & Discussion

4.1 Physical Characteristics

Fig. 5a shows the SEM images of graphene platelets (highlighted in yellow) found on the samples, indicating that they had been successfully incorporated into the final printed structure. The temperature sweep results from the DSC and DMA testing (adapted from Ref. [15]) are shown in Fig. 5b and 5c respectively. The DSC curves indicate that there was an acceleration of endothermic reactions in the material for ≥ 50 °C for the 3D printed neat polymer without post-print bake, and ≥ 40 °C for the rest of the samples (indicated as '**V**' in Fig. 5b). These reactions were accompanied by a rapid increase in viscous losses when the materials were subjected to mechanical deformation (Fig. 5c).

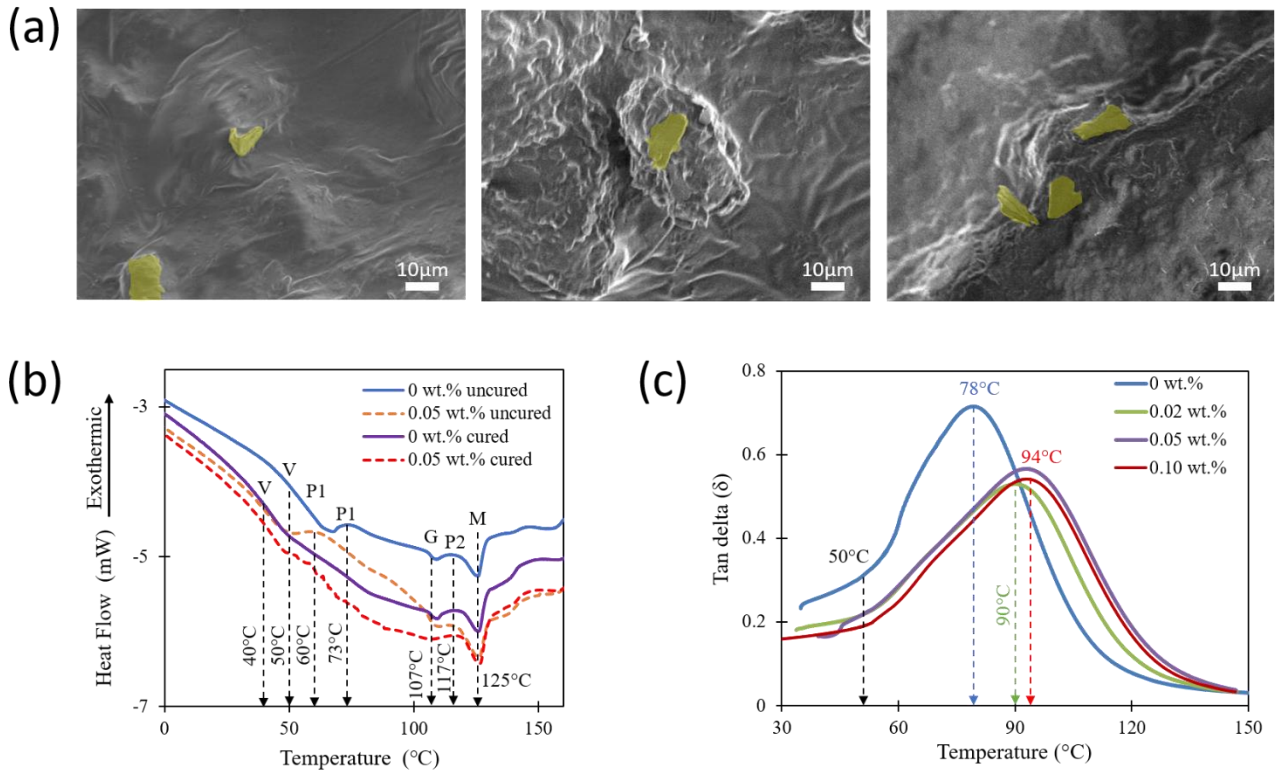

Figure 5: (a) SEM images of the graphene platelets (yellow) found on the surface of the 3D printed graphene-polymer nanocomposites. (b) DSC analysis of a 3D printed neat Grey Resin polymer and a nanocomposite that had 0.05 wt.% of graphene content. For each sample, the DSC curves before and after post-print baking at 120 °C for 60 min were obtained. (c) DMA results (adapted from Ref. *[15]*) **showing tan** δ **(*i.e.* ratio of loss modulus to storage modulus) of the nanocomposites with different graphene content. 0 wt.% graphene refers to the neat Grey Resin polymer. These samples had been subjected to post-print bake at 120 °C for 60 min.**

For the uncured samples, this was followed immediately by a broad exothermic peak at 73 °C for the neat polymer and at 60 °C for the graphene-polymer nanocomposite (indicated as '**P1**' in Fig. 5b). These peaks were not observed for the samples that had undergone post-print baking at 120°C for 60 min. This result, which is consistent with previous DSC data on PMMA resin powder[43], suggests that the exothermic peaks were caused by methyl methacrylate (MMA) polymerization reactions [44].

This conclusion is further supported by previous observations that the degree of cure in as-printed Grey Resin is only 60% - 80% and requires a post-print bake to cross 90% [31]. The same study also noted that the as-printed graphene nanocomposites tend to be less polymerized than the neat polymer due to graphene's strong absorbance of the laser light, which may explain why phases **V** and **P1** appear to occur at a lower temperature for the graphene nanocomposites.

At 107 °C (denoted as '**G**' in Fig. 5b), the samples appeared to undergo glass transition. It had been suggested previously that the temperature for the onset of phase **V** was the glass transition temperature (T_g) for Grey Resin [18] and that reinforced PMMA may have 2 distinct glass transition temperatures, 1 corresponding to the neat polymer at ~ 60 °C and another for the polymer encased filler particles at ~ 120 °C [45]. Based on the DMA results in Fig. 5c, however, it appears that phases **V** and **G** were part of the same glass transition process and the temperature. Furthermore, the temperature for phase **G** is more consistent with the T_g obtained through DMA testing. The slight difference in T_g measured through DSC and DMA can be attributed to the different measurement principles and is well-documented for PMMA [17], a major component of Grey Resin [15].

As the temperature increased beyond T_g, a second exothermic peak ('**P2**' in Fig. 5b) was observed at 117 °C. Similar to **P1**, these peaks were significantly more pronounced for the samples without post-print bake, indicating that they were, again, due to MMA polymerization reactions, which may have been accelerated as the bonds between the polymer chains loosened, reducing steric hindrance and allowing unreacted monomers to diffuse and react with each other [31,46]. Finally, a sharp endothermic peak at 125 °C ('**M**' in Fig. 5b) for all the samples suggests that melting may have occurred.

The DMA results generally support the inferences drawn from the DSC testing. While it was not able to identify the multiple physical processes occurring in the material, it could resolve the T_g in better detail. From Fig. 5b, it can be observed that as the graphene concentration increased from 0

wt.% to 0.05 wt.%, T_g increased from 78 °C to 94 °C. In addition, the peak values of tan δ, which represents the ratio of loss modulus to storage modulus, were noticeably lower for the graphene nanocomposites than neat polymer. These results indicate that the graphene platelets were able to effectively restrict the movement of the polymer chains [18,47,48], so that viscous loss was reduced for a given temperature, *i.e.* a higher temperature is required to obtain the same viscous loss. This implies that there was good interfacial bonding between the graphene platelets and polymer matrix, which is important for load transfer from the polymer matrix to graphene.

4.2 Dynamic Modulus: Effect of Printing Axis

Fig. 6 shows the DMA frequency sweep results for different printing orientations. While the storage modulus of the neat polymer (0 wt.% graphene) was independent of the printing direction (*i.e.* the printed neat polymer had isotropic properties), the cuboid structure printed in the axis parallel to its length consistently showed the highest storage modulus for the graphene nanocomposites (0.02 wt.% to 0.10 wt.%). The storage moduli for the other 2 printing directions, on the other hand, were similar to each other. These results ruled out the possibility that graphene addition caused a layered microstructure to form during 3D printing of the nanocomposites and the anisotropy in properties resulted from weak interlayer bonding. If that was true, the storage modulus should have been higher in the 'breadth' and 'height' printing directions, which is contrary to observation.

To calculate the modulus-frequency trends for the graphene nanocomposites using the quantitative model, the experimental data for the neat polymer was first fitted to the Maxwell material equations (Eq. 9 and 10). Using the empirically obtained E_p (~ 2.4 GPa) and η_p (~ 0.55 GPa.s), and taking E_g = 1 TPa, the moduli of the graphene nanocomposites with respect to frequency were obtained and plotted in Fig. 6. Some deviations between the experimental and theoretical curves, particularly for the loss modulus, are expected due to the highly simplified linear viscoelastic models employed.

Nevertheless, the calculated trends from these basic models agreed reasonably well with the experimental data, allowing a few key predictions to be made.

Firstly, the storage modulus follows a logarithmic asymptotic trend with respect to frequency. Mathematically, Eq. (9), (14) and (21) indicate that a high frequency would cancel out the viscous effects of η_p, allowing E' to rise towards an asymptotic value. Physically, this result can be understood by realizing that a higher vibrational frequency implies a greater strain rate. When the molecular chains in the polymer matrix were stressed rapidly, they were not given sufficient time to enact significant entropic and/ or conformational changes (*e.g.* 'sliding' of polymer chains past each other) that would lead to dissipation of the mechanical energy as heat (*i.e.* viscous losses) [49]. Instead, the polymer could only exhibit limited deformation through reversible, elastic bond stretching [49]. Therefore, as the strain rate rose, the storage modulus of the polymer increased. The asymptotic value is achieved when the polymer deformation was completely dominated by the bond stretching mechanism.

Secondly, the storage modulus for a given frequency increased with graphene concentration. With more graphene, more of the applied load was transferred to the stiffer graphene platelets, allowing the overall storage modulus of the nanocomposite to increase. The effectiveness of this stress transfer also indicates that there was good bonding between the PMMA and graphene platelets.

Thirdly, the loss modulus was largely independent of frequency, print orientation and even graphene concentration. Eq. (15) and (22) indicate that when $f_p \rightarrow 1$ (*i.e.* dilute filler concentrations) and $E_p >> \eta_p$ (storage modulus of polymer matrix is much higher than loss modulus), as is the case for Grey Resin here, E'' converges to $E_p^2/(\omega\eta_p)$ at large ω ($> 20\pi$ rad /s), regardless of the orientation of the graphene platelets in the polymer matrix. Essentially, since the filler concentration was so low, the viscous losses originated only from the polymer matrix, and therefore, the orientation of the reinforcement filler becomes unimportant. Furthermore, at high frequencies/ strain rates, permanent changes in the shape and arrangement of polymer chains do not have sufficient time to occur, as discussed above, and therefore, the loss modulus plateaued rapidly.

Comparing the experimental data to theoretical predictions, it can also be observed that the storage modulus for samples printed along their length tend to follow the predicted values for the isostrain geometry. The trends for nanocomposites printed along the breadth and height axes, on the other hand, lie between the isostress and isostrain curves, suggesting that some of the graphene platelets were oriented in the isostrain orientation, and the rest, in the isostress orientation. This result agrees well with the qualitative predictions of the graphene platelet orientations set forth in Fig. 2b and provides compelling evidence for the SNAG process. It is worth mentioning that we have made attempts to directly observe the orientations of the graphene in the composite through micro-CT scanning, but we were unable to obtain useful results due to insufficient contrast between the graphene platelets and polymer matrix.

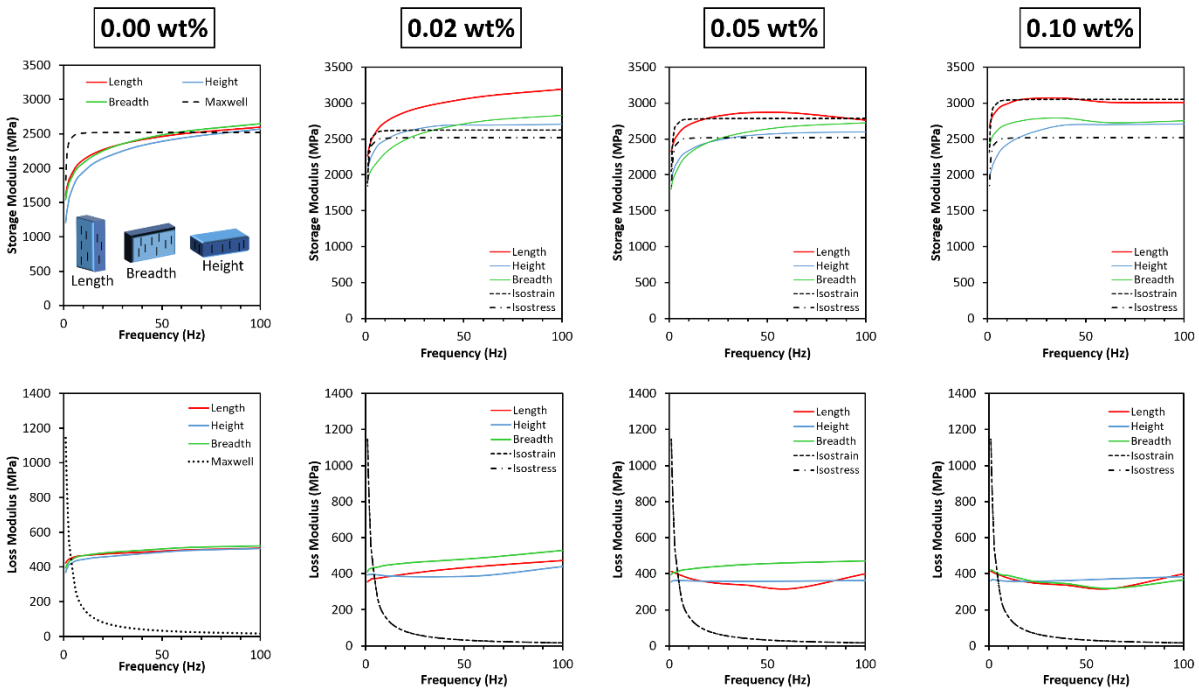

Figure 6: Effect of print orientation on the storage modulus, *E′*, and loss modulus, *E″*, of the graphene-polymer nanocomposites baked at 120 °C for 60 min after 3D printing.

4.3 Dynamic Modulus: Effect of Graphene Concentration and Post-Print Baking Temperature

Fig. 7 shows the dynamic modulus of the samples for different graphene concentrations and post-print baking temperature. The printing axis of these samples was aligned to the length of the cuboids. The results show that the storage modulus, E', of the polymer increased with increasing graphene concentration, which is consistent with the results in Fig. 6. E' also increased with the temperature of the post-print bake up to 120°C, but fell when the temperature was increased to 160°C, regardless of graphene content. This is because PMMA, the main component of Grey Resin, begins to degrade above 150°C [17,50], primarily due to the scission of bonds generated between active polymer chains during combination termination [50].

Similar to the results in Fig. 6, E' of the nanocomposites was observed to follow the trend of the isostrain predictions reasonably well, and the loss modulus, E'', was, once again, much lower than E' and relatively independent of the graphene concentration, post-print bake temperature and test frequency. Nevertheless, E'' was able to remain at approximately 10% of the value of E', endowing the nanocomposites with vibration damping abilities 10 times better than graphene - coated nickel foams [51] and comparable to coconut sheath/glass fiber/nano-clay reinforced hybrid polyester composite [52].

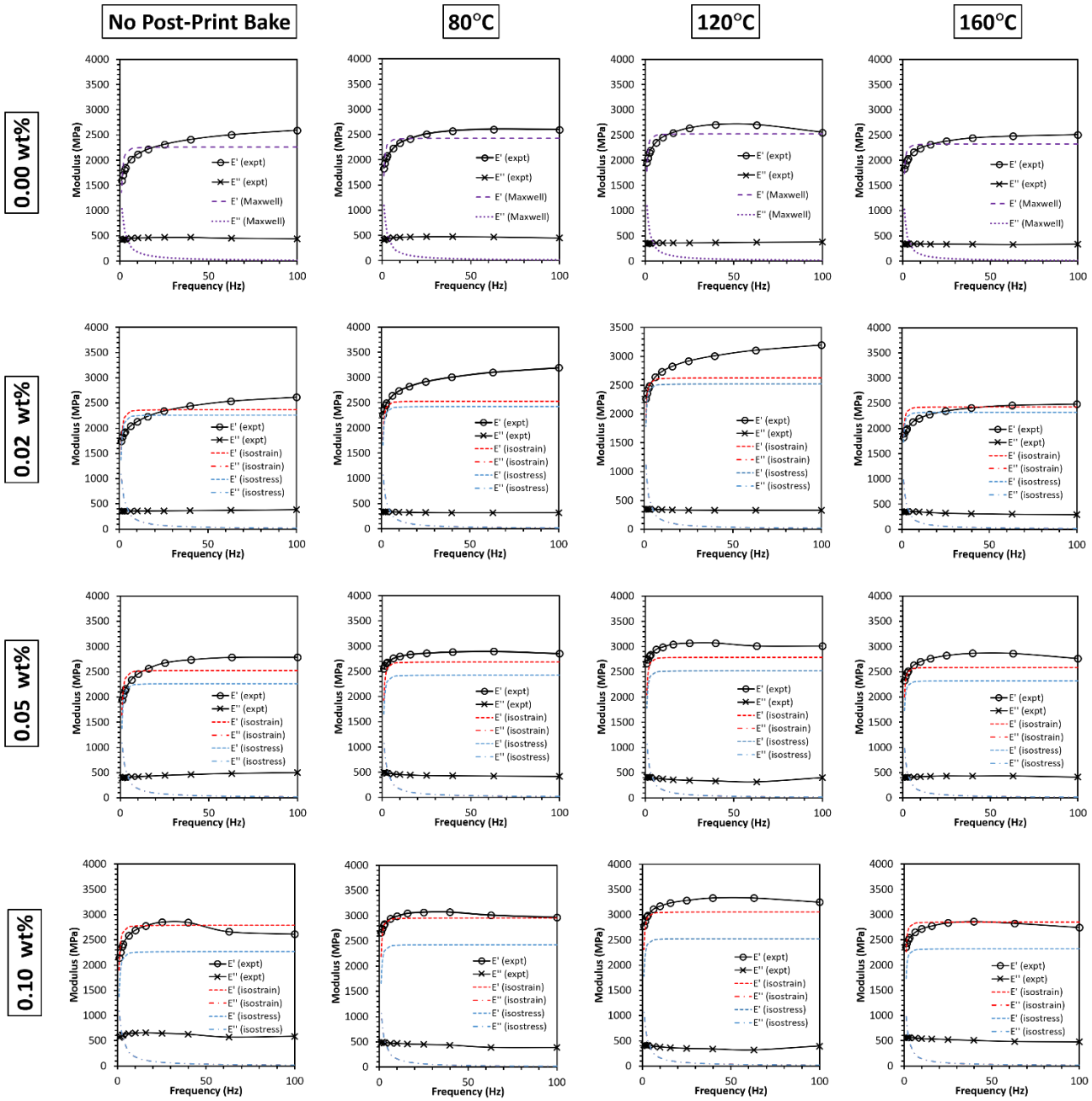

Figure 7: Effect of post-print baking temperature and graphene content on the storage modulus, *E′*, and loss modulus, *E″*, of the 3D printed graphene-polymer nanocomposites.

4.4 Dynamic Strength: Effect of Graphene Content and Post-Print Bake Temperature

The graphene nanocomposites were 3D printed so that the graphene platelets would adopt an isostrain orientation (Fig. 8a inset), as this arrangement is expected to offer the highest possible failure stresses. The strength of the graphene nanocomposites was then investigated under high strain rate loading.

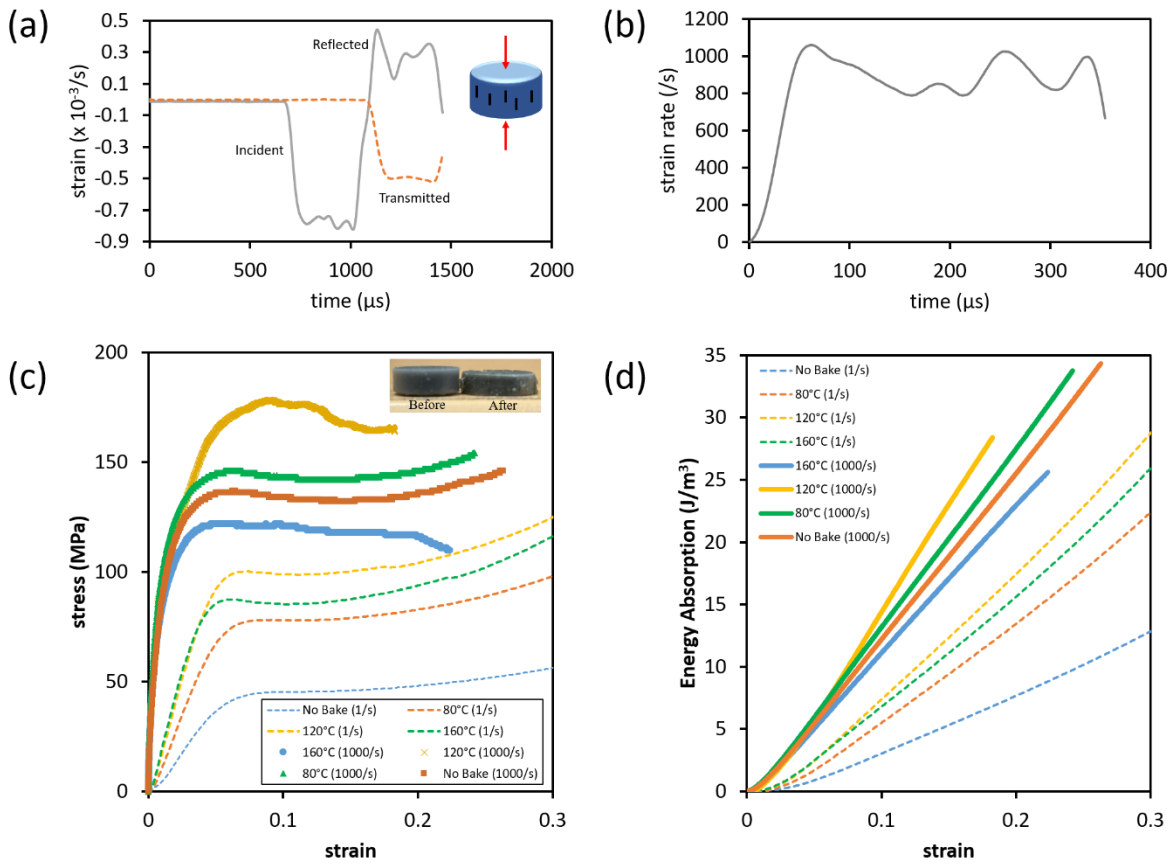

Figure 8: (a) A typical set of compressive waveforms captured by the strain gauges in the Split-Hopkinson pressure bar test. (b) The time-resolved strain rate applied on the sample, calculated from part (a). (c) Dynamic engineering stress-strain response of graphene nanocomposite at low (1 /s) and high (1000 /s) strain rates. The nanocomposites contained 0.05 wt.% of graphene and were subjected to 60 min post-print bake at different temperatures. (Inset) Images of the samples before and after high strain rate

compression test. (d) Energy absorption per unit volume vs. strain trends derived from part (c).

Fig. 8a shows a typical example of the incident, reflected and transmitted compression waves captured by the mounted strain gauges. Using the 1D stress wave theory and assuming stress equilibrium was achieved, the strain rate, $\dot{\varepsilon}$, engineering stress, σ, and engineering strain, ε, can be computed as follows [36,53],

$$\dot{\varepsilon}(t) = \frac{2C_B}{H_s}\varepsilon_R(t) \tag{27}$$

$$\sigma = \frac{A_B E_B}{A_s}\varepsilon_T(t) \tag{28}$$

$$\varepsilon(t) = \frac{2C_B}{H_s}\int_0^t \varepsilon_R(t)\,dt \tag{29}$$

C_B, E_B, and A_B refer to the sound velocity, Young's modulus and cross-sectional area of the bars respectively. H_s and A_s refer to the height and cross-sectional area of the sample, while t refers to time. ε_R and ε_T refer to the time-resolved strains caused by the reflected and transmitted compression waves respectively.

Using Eq. (27), the strain data in Fig. 8a can be converted into the time-resolved strain rate applied to the sample (Fig. 8b), which can be observed to be fairly consistent (~ 900 /s) over the duration of the experiment. With Eq. (28) and (29), the dynamic stress-strain response of the sample can be obtained as shown in Fig. 8c. The stress-strain responses of the same samples at a much lower strain rate (1 /s) are included for comparison.

Regardless of the strain rate, the general stress-strain response of the graphene nanocomposites was the same, beginning with a steep, linear elastic regime and then plateauing after reaching the failure stress. Such a response suggests that the 3D printed graphene nanocomposites deform mainly by ductile yielding (Fig. 8c). In addition, for both strain rates, the failure and plateau stress of the Grey Resin polymer improved with increasing post-print

bake temperature up to 120 °C, and then decreased when the temperature was further raised to 160 °C. This is due to the aforementioned degradation of the PMMA in Grey Resin when the bake temperature exceeds 150 °C [17,50].

The failure stress and energy absorption of the graphene nanocomposites at a strain rate of 1000 /s were, respectively, found to be ~ 1.75 times and up to ~ 3 times that at a strain rate of 1 /s (Fig. 8c and 8d), indicating that the graphene nanocomposites had considerably better impact absorption capability than their quasistatic values suggest. In addition, after baking at 120 °C, the graphene nanocomposites exhibited a failure stress that was ~ 1.5 times and energy absorption up to ~ 1.4 times that of the unbaked composite at a strain rate of 1000 /s (Fig. 8c and 8d). This strength and energy absorption enhancements were fairly consistent across the graphene concentrations, except at 0.10 wt. % (Fig. 9).

It is also clear from Fig. 9 that Eq. (26) predicts a linear relationship between the dynamic strength of the nano composites and the graphene concentration, f_g, which generally agrees well with the experimental data. The implication of this good fit is that failure of the graphene nanocomposites was indeed initiated by failure in the polymer matrix, as assumed in the derivation of Eq. (26). This is to be expected, since graphene has a much higher failure strength (~130 GPa) [3] than the polymer (~100 MPa) [15] and the graphene-PMMA bonding is generally quite strong [21,42], making it highly unlikely for the failure source to be the graphene platelets or graphene-polymer interfaces.

The main exception to the above result occurred when the graphene concentration was 0.10 wt.% (Fig. 9). The experimentally obtained peak stress was significantly lower than the predicted value, suggesting that the failure mode may have changed. It had previously been observed that at 0.10 wt.% of graphene concentration, the graphene platelets prepared using

the method in this study led to agglomeration [15]. The weak bonding between the platelets could, therefore, be a source of premature failure.

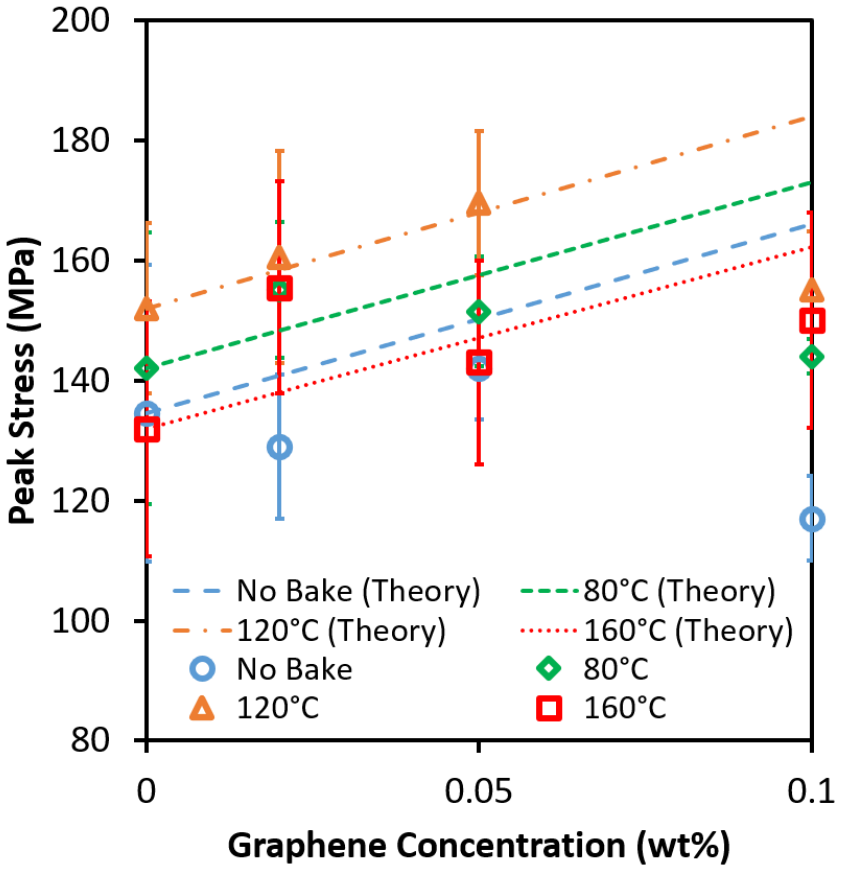

Figure 9: Experimental and calculated values of the peak stress (*i.e.* dynamic failure strength) of neat polymer (0 wt. % graphene) and graphene nanocomposites for different post-print bake temperatures. The baking duration was 60 min. The theoretical trend for each bake temperature was obtained by entering the empirical value of the neat polymer's peak stress into Eq. (26) as σ_p. The error bars indicate the standard deviations.

4.5 Lattices

The enhancement in dynamic strength of Grey Resin from small additions of graphene was not limited only to 3D printed bulk samples, but can be extended to complex lattices that

were fabricated with the same stereolithography method as well. Fig. 10 shows the DMA test results of a simple cubic lattice in a cuboid form factor. As with the bulk samples, the storage modulus, E', is clearly observed to improve by ~ 40% with the addition of 0.02 wt.% of graphene or when the samples were subjected to 120°C of post-print baking for 60 min. If both treatments are applied, E' of the graphene nanocomposite can improve nearly 100% over the unbaked neat polymer at 100 Hz. The loss modulus, E'', was, once again, observed to be independent of the frequency, bake temperature and graphene concentration, remaining at ~ 10% of E' (*i.e.* tan $\delta \sim 0.1$), indicating that the lattice had a fair amount of vibration damping capacity comparable to the bulk samples.

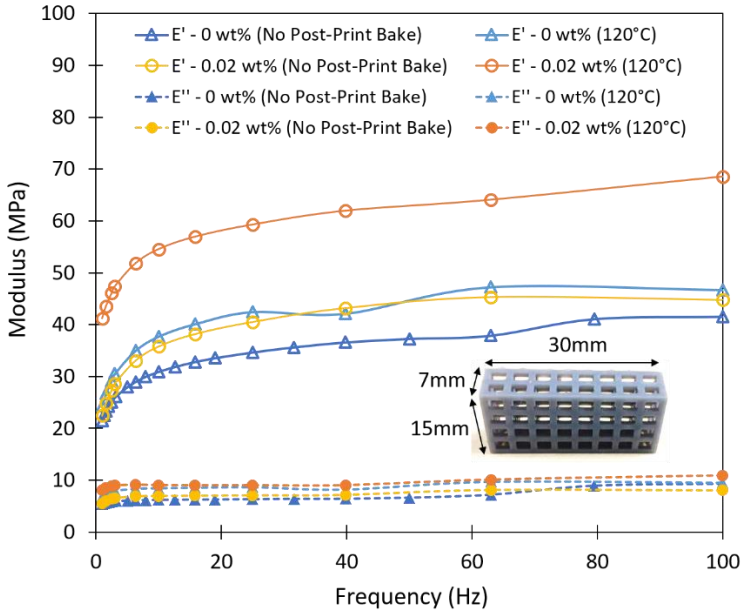

Figure 10: DMA test results showing the storage modulus, E', and loss modulus, E'', of a simple cubic lattice with different graphene concentrations and post-print heat treatment. (Inset) Photograph of the cuboid-shaped simple cubic lattice and the relevant dimensions. The truss width was 1 mm and the relative density was 0.2. The print axis was parallel to the length of the cuboid.

Fig. 11 shows the dynamic stress-strain response and energy absorption characteristics of Octet Truss lattices fabricated out of the neat polymer and with 0.02 wt. % of graphene added via the SNAG process during 3D printing. In line with the results obtained for bulk samples, the addition of graphene and/ or post-print bake produced an evident improvement of the dynamic strength and impact energy absorption capability of the lattice.

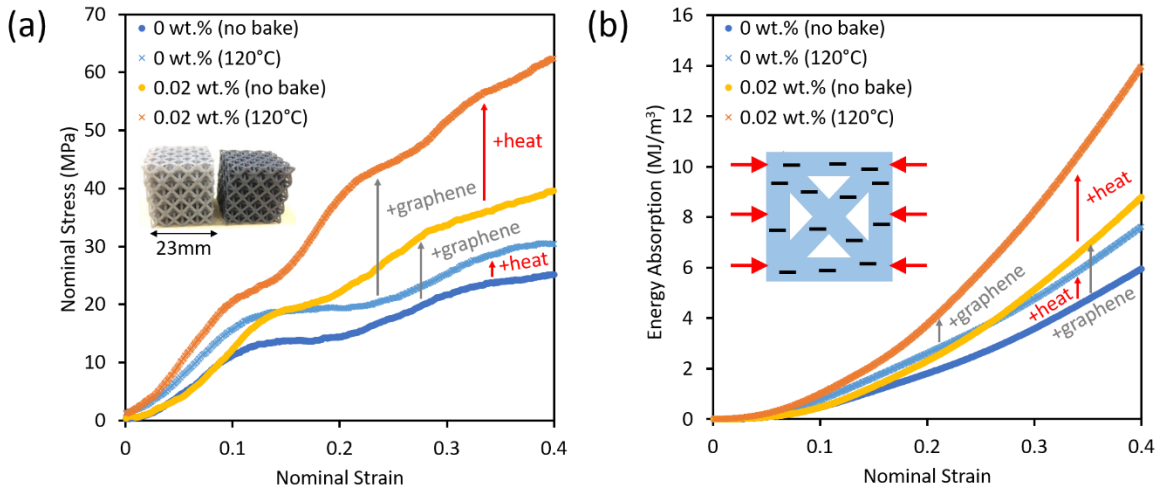

Figure 11: (a) Dynamic stress-strain response of Octet Truss lattices with different graphene concentrations and post-print heat treatments. (Inset) Photograph of the neat polymer (left) and graphene nanocomposite (right) lattice. The truss width was 1 mm and the relative density was 0.31. (b) Energy absorption per unit volume of the Octet Truss lattices. The trends were derived from area under the curves in (a). (Inset) Schematic diagram illustrating the orientation of the graphene platelets (black) in the lattice (blue) with respect to the loading direction (red).

4.6 Comparison with Other Structural Materials

To evaluate the performance of the graphene nanocomposites, we compared their dynamic properties against those of other popular structural materials. From Fig. 12, it is clear

that at high strain rate (~ 1000/s), the 3D printed aligned-graphene nanocomposites significantly outperformed most solid Al alloys and foams in specific strength, exhibiting values comparable to the best reported in the literature for non-additively-manufactured graphene – polymer and carbon nanotube – polymer composites, which typically incorporate a much higher concentration of fillers (0.1 – 7.5 wt.%). In addition, the graphene nanocomposite lattices also showed better energy absorption per unit weight than Al foams and porous ceramics, such as A&T's Eco-core (Fig. 12b). For instance, the Octet Truss lattice with 0.02 wt.% of graphene content had an energy absorption per unit mass of 38.9 kJ/kg, which is nearly twice that of the 22 kJ/kg exhibited by the next best porous material, Balsa wood [55].

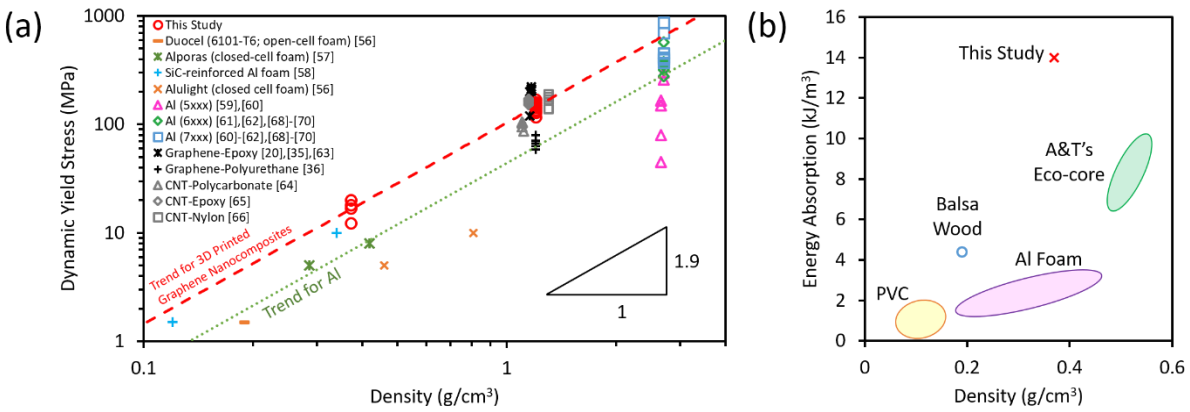

Figure 12: Comparison of the (a) dynamic strength vs. density (b) energy absorption vs. density characteristics of the 3D printed aligned graphene nanocomposites against other lightweight engineering materials – Duocel *[56]*, **Alporas** *[57]*, **SiC-reinforced Al foam** *[58]*, **Alulight** *[56]*, **Al (5xxx)** *[59,60]*, **Al (6xxx)** *[61,62]*, **Al (7xxx)** *[60–62]*, **non-3D-printed graphene-polymer composites** *[20,35,36,63]*, **non-3D-printed carbon nanotube (CNT)-polymer composites** *[64–66]* **and common porous core materials** *[55,67]*. **High strain rate tensile test results for Al alloys are plotted in (a) as well** *[68–70]*. **Only literature data obtained at a strain rate similar to that used in the present study (~ 1000 /s) have been included.**

5. Conclusions

The time-dependent mechanical properties of stereolithographically 3D printed graphene-polymer composites were investigated through dynamic mechanical analysis (DMA) and the use of the Split-Hopkinson pressure bar (SHPB). It was found that the storage modulus and dynamic failure strength of the nanocomposites improved monotonically with higher graphene content, indicating that there was increasing load transfer to graphene. This implied that there was a strong interfacial bonding between the graphene and polymer, which comprised primarily of PMMA. However, at a graphene concentration of 0.10 wt.%, the strength of the nanocomposite worsened, possibly because of the presence of weak interfaces generated by graphene platelet agglomeration. As a result, failure in these nanocomposites would initiate in these interfaces, rather than primarily in the polymers, which was the case when the graphene content was $\leq$ 0.05 wt.%. The nanocomposites were also found to exhibit a higher storage modulus and strength after a 60 min post-print bake up to 120 °C, which improved the degree of cure in the polymer. At 160 °C, however, the storage modulus worsened due to polymer degradation.

The good graphene-polymer interfacial bonding up to 0.05 wt.% of graphene and improved degree of cure up to 120 °C were qualitatively supported by results from differential scanning calorimetry and DMA temperature sweep, which indicated a rise in glass transition temperature with the addition of graphene platelets. Similar results pertaining to graphene content and post-print baking were observed with complex 3D lattices fabricated using the same technique. In addition, we showed that the influence of graphene concentration and post-print bake on the dynamic modulus and strength of the graphene nanocomposites could be

described reasonably well by semi-empirical relationships derived from simple viscoelastic models.

Furthermore, DMA testing of nanocomposites printed along different axes confirmed, indirectly, that 3D stereolithography printing of graphene-polymer resin resulted in the alignment of graphene platelets along the print axis, lending support to the previously proposed SNAG (Self-selection of Naturally Aligned Graphene) process. Therefore, when the nanocomposite is loaded in an axis parallel to the print axis, the composite adopts an isostrain geometry, which offers high dynamic modulus and strength. This was further confirmed through extensive testing of the graphene nanocomposites in the DMA frequency sweep mode.

The dynamic properties of the graphene-polymer nanocomposites were compared with that of other lightweight structural materials, such as Al alloys, Al foams, Balsa wood, syntactic ceramic foams, as well as graphene – polymer and carbon nanotube – polymer composites fabricated with non-additive-manufacturing techniques, and it was found that the nanocomposites outperformed almost all of these materials on a per unit mass basis. This result is all the more remarkable when considering the low concentrations of graphene utilized in the nanocomposites ($\leq$ 0.10 wt.%).

6. Acknowledgements

The authors would like to acknowledge funding for this project by the Temasek Research Fellowship, which C.Q.L is grateful for.

References

[1] K.S. Novoselov, Z. Jiang, Y. Zhang, S.V. Morozov, H.L. Stormer, U. Zeitler, J.C. Maan, G.S. Boebinger, P. Kim, A.K. Geim, Room-Temperature Quantum Hall Effect in Graphene, Science. (2007) 1137201. https://doi.org/10.1126/science.1137201.

[2] Y. Zhang, Y.-W. Tan, H.L. Stormer, P. Kim, Experimental observation of the quantum Hall effect and Berry's phase in graphene, Nature. 438 (2005) 201–204. https://doi.org/10.1038/nature04235.

[3] C. Lee, X. Wei, J.W. Kysar, J. Hone, Measurement of the Elastic Properties and Intrinsic Strength of Monolayer Graphene, Science. 321 (2008) 385–388. https://doi.org/10.1126/science.1157996.

[4] A.A. Balandin, S. Ghosh, W. Bao, I. Calizo, D. Teweldebrhan, F. Miao, C.N. Lau, Superior Thermal Conductivity of Single-Layer Graphene, Nano Letters. 8 (2008) 902–907. https://doi.org/10.1021/nl0731872.

[5] R.R. Nair, P. Blake, A.N. Grigorenko, K.S. Novoselov, T.J. Booth, T. Stauber, N.M.R. Peres, A.K. Geim, Fine Structure Constant Defines Visual Transparency of Graphene, Science. 320 (2008) 1308–1308. https://doi.org/10.1126/science.1156965.

[6] K.S. Novoselov, A.K. Geim, S.V. Morozov, D. Jiang, Y. Zhang, S.V. Dubonos, I.V. Grigorieva, A.A. Firsov, Electric Field Effect in Atomically Thin Carbon Films, Science. 306 (2004) 666–669. https://doi.org/10.1126/science.1102896.

[7] K.S. Novoselov, A.K. Geim, S.V. Morozov, D. Jiang, M.I. Katsnelson, I.V. Grigorieva, S.V. Dubonos, A.A. Firsov, Two-dimensional gas of massless Dirac fermions in graphene, Nature. 438 (2005) 197–200. https://doi.org/10.1038/nature04233.

[8] V. Georgakilas, M. Otyepka, A.B. Bourlinos, V. Chandra, N. Kim, K.C. Kemp, P. Hobza, R. Zboril, K.S. Kim, Functionalization of Graphene: Covalent and Non-Covalent Approaches, Derivatives and Applications, Chem. Rev. 112 (2012) 6156–6214. https://doi.org/10.1021/cr3000412.

[9] C.S. Boland, U. Khan, M. Binions, S. Barwich, J.B. Boland, D. Weaire, J.N. Coleman, Graphene-coated polymer foams as tuneable impact sensors, Nanoscale. 10 (2018) 5366–5375. https://doi.org/10.1039/C7NR09247D.

[10] N. Yousefi, X. Sun, X. Lin, X. Shen, J. Jia, B. Zhang, B. Tang, M. Chan, J.-K. Kim, Highly Aligned Graphene/Polymer Nanocomposites with Excellent Dielectric Properties for High-Performance Electromagnetic Interference Shielding, Advanced Materials. 26 (2014) 5480–5487. https://doi.org/10.1002/adma.201305293.

[11] D.W. Chang, H.-J. Choi, A. Filer, J.-B. Baek, Graphene in photovoltaic applications: organic photovoltaic cells (OPVs) and dye-sensitized solar cells (DSSCs), J. Mater. Chem. A. 2 (2014) 12136–12149. https://doi.org/10.1039/C4TA01047G.

[12] T.A. Amollo, G.T. Mola, V.O. Nyamori, High-performance organic solar cells utilizing graphene oxide in the active and hole transport layers, Solar Energy. 171 (2018) 83–91. https://doi.org/10.1016/j.solener.2018.06.068.

[13] M. Li, X. Yang, J. Ren, K. Qu, X. Qu, Using Graphene Oxide High Near-Infrared Absorbance for Photothermal Treatment of Alzheimer's Disease, Advanced Materials. 24 (2012) 1722–1728. https://doi.org/10.1002/adma.201104864.

[14] J.T. Robinson, S.M. Tabakman, Y. Liang, H. Wang, H. Sanchez Casalongue, D. Vinh, H. Dai, Ultrasmall Reduced Graphene Oxide with High Near-Infrared Absorbance for Photothermal Therapy, J. Am. Chem. Soc. 133 (2011) 6825–6831. https://doi.org/10.1021/ja2010175.

[15] K. Markandan, C.Q. Lai, Enhanced mechanical properties of 3D printed graphene-polymer composite lattices at very low graphene concentrations, Composites Part A: Applied Science and Manufacturing. 129 (2020) 105726. https://doi.org/10.1016/j.compositesa.2019.105726.

[16] T.K. Das, S. Prusty, Graphene-Based Polymer Composites and Their Applications, Polymer - Plastics Technology and Engineering. 52 (2013) 319–331. https://doi.org/10.1080/03602559.2012.751410.
[17] T. Kuila, S. Bose, P. Khanra, N.H. Kim, K.Y. Rhee, J.H. Lee, Characterization and properties of in situ emulsion polymerized poly(methyl methacrylate)/graphene nanocomposites, Composites Part A: Applied Science and Manufacturing. 42 (2011) 1856–1861. https://doi.org/10.1016/j.compositesa.2011.08.014.
[18] J.Z. Manapat, J.D. Mangadlao, B.D.B. Tiu, G.C. Tritchler, R.C. Advincula, High-Strength Stereolithographic 3D Printed Nanocomposites: Graphene Oxide Metastability, ACS Appl. Mater. Interfaces. 9 (2017) 10085–10093. https://doi.org/10.1021/acsami.6b16174.
[19] N. Pandey, C. Tewari, S. Dhali, B.S. Bohra, S. Rana, S.P.S. Mehta, S. Singhal, A. Chaurasia, N.G. Sahoo, Effect of graphene oxide on the mechanical and thermal properties of graphene oxide/hytrel nanocomposites, Journal of Thermoplastic Composite Materials. (2019) 1–13. https://doi.org/10.1177/0892705719838010.
[20] S.A. Bansal, A.P. Singh, S. Kumar, High Strain Rate Behavior of Epoxy Graphene Oxide Nanocomposites, Int. J. Appl. Mechanics. 10 (2018) 1850072. https://doi.org/10.1142/S1758825118500722.
[21] D.G. Papageorgiou, I.A. Kinloch, R.J. Young, Mechanical properties of graphene and graphene-based nanocomposites, Progress in Materials Science. 90 (2017) 75–127. https://doi.org/10.1016/j.pmatsci.2017.07.004.
[22] J.W. Suk, R.D. Piner, J. An, R.S. Ruoff, Mechanical Properties of Monolayer Graphene Oxide, ACS Nano. 4 (2010) 6557–6564. https://doi.org/10.1021/nn101781v.
[23] M.A. Rafiee, J. Rafiee, Z. Wang, H. Song, Z.-Z. Yu, N. Koratkar, Enhanced Mechanical Properties of Nanocomposites at Low Graphene Content, ACS Nano. 3 (2009) 3884–3890. https://doi.org/10.1021/nn9010472.
[24] J. Zhong, A.I. Isayev, X. Zhang, Ultrasonic twin screw compounding of polypropylene with carbon nanotubes, graphene nanoplates and carbon black, European Polymer Journal. 80 (2016) 16–39. https://doi.org/10.1016/j.eurpolymj.2016.04.028.
[25] H. Guo, R. Lv, S. Bai, Recent advances on 3D printing graphene-based composites, Nano Materials Science. 1 (2019) 101–115. https://doi.org/10.1016/j.nanoms.2019.03.003.
[26] K. Gnanasekaran, T. Heijmans, S. van Bennekom, H. Woldhuis, S. Wijnia, G. de With, H. Friedrich, 3D printing of CNT- and graphene-based conductive polymer nanocomposites by fused deposition modeling, Applied Materials Today. 9 (2017) 21–28. https://doi.org/10.1016/j.apmt.2017.04.003.
[27] D. Zhu, Y. Ren, G. Liao, S. Jiang, F. Liu, J. Guo, G. Xu, Thermal and mechanical properties of polyamide 12/graphene nanoplatelets nanocomposites and parts fabricated by fused deposition modeling, Journal of Applied Polymer Science. 134 (2017) 45332. https://doi.org/10.1002/app.45332.
[28] Z. Feng, Y. Li, C. Xin, D. Tang, W. Xiong, H. Zhang, Fabrication of Graphene-Reinforced Nanocomposites with Improved Fracture Toughness in Net Shape for Complex 3D Structures via Digital Light Processing, C — Journal of Carbon Research. 5 (2019) 25. https://doi.org/10.3390/c5020025.
[29] Z. Çiplak, N. Yildiz, A. Çalimli, Investigation of Graphene/Ag Nanocomposites Synthesis Parameters for Two Different Synthesis Methods, Fullerenes, Nanotubes and Carbon Nanostructures. 23 (2015) 361–370. https://doi.org/10.1080/1536383X.2014.894025.
[30] C.H.A. Tsang, A. Zhakeyev, D.Y.C. Leung, J. Xuan, GO-modified flexible polymer nanocomposites fabricated via 3D stereolithography, Front. Chem. Sci. Eng. 13 (2019) 736–743. https://doi.org/10.1007/s11705-019-1836-x.
[31] A.S. de León, S.I. Molina, Influence of the Degree of Cure in the Bulk Properties of Graphite Nanoplatelets Nanocomposites Printed via Stereolithography, Polymers. 12 (2020) 1103. https://doi.org/10.3390/polym12051103.

[32] H. Sun, Z. Xu, C. Gao, Multifunctional, Ultra-Flyweight, Synergistically Assembled Carbon Aerogels, Advanced Materials. 25 (2013) 2554–2560. https://doi.org/10.1002/adma.201204576.
[33] F. Wang, H. Wang, J. Mao, Aligned-graphene composites: a review, J Mater Sci. 54 (2019) 36–61. https://doi.org/10.1007/s10853-018-2849-4.
[34] D. Li, Y. Liu, H. Ma, Y. Wang, L. Wang, Z. Xie, Preparation and properties of aligned graphene composites, RSC Adv. 5 (2015) 31670–31676. https://doi.org/10.1039/C5RA03486H.
[35] Ö.U. Colak, N. Bahlouli, D. Uzunsoy, C. Francart, High strain rate behavior of graphene-epoxy nanocomposites, Polymer Testing. 81 (2020) 106219. https://doi.org/10.1016/j.polymertesting.2019.106219.
[36] S.K. Khanna, H.T.T. Phan, High Strain Rate Behavior of Graphene Reinforced Polyurethane Composites, J. Eng. Mater. Technol. 137 (2015). https://doi.org/10.1115/1.4029291.
[37] G.Y. Baghdasaryan, M.A. Mikilyan, R.O. Saghoyan, E. Cestino, G. Frulla, P. Marzocca, Nonlinear LCO “amplitude–frequency” characteristics for plates fluttering at supersonic speeds, International Journal of Non-Linear Mechanics. 77 (2015) 51–60. https://doi.org/10.1016/j.ijnonlinmec.2015.06.014.
[38] I.-L. Yeh, N. Elangovan, R. Feczer, S. Khosravani, A. Mahnan, J. Konczak, Vibration-Damping technology in tennis racquets: Effects on vibration transfer to the arm, muscle fatigue and tennis performance, Sports Medicine and Health Science. 1 (2019) 49–58. https://doi.org/10.1016/j.smhs.2019.09.001.
[39] M. Jawaid, M. Thariq, N. Saba, Modelling of Damage Processes in Biocomposites, Fibre-Reinforced Composites and Hybrid Composites, Woodhead Publishing, 2018.
[40] J. Worobets, D. Stefanyshyn, The influence of golf club shaft stiffness on clubhead kinematics at ball impact, Sports Biomech. 11 (2012) 239–248. https://doi.org/10.1080/14763141.2012.674154.
[41] S. Patra, V.T. Veettil, T.N. Narayanan, Enhanced viscoelastic properties of graphene oxide membranes, Carbon. 124 (2017) 576–583. https://doi.org/10.1016/j.carbon.2017.09.017.
[42] I. Seetoh, K. Markandan, C.Q. Lai, Effect of reinforcement bending on the elastic properties of interpenetrating phase composites, Mechanics of Materials. 136 (2019) 103071. https://doi.org/10.1016/j.mechmat.2019.103071.
[43] A. Ohyama, Y. Imai, Differential scanning calorimetric study of acrylic resin powders used in dentistry, Dent Mater J. 19 (2000) 346–351. https://doi.org/10.4012/dmj.19.346.
[44] S.-M. Ahn, S.-C. Chang, H.-K. Rhee, Application of optimal temperature trajectory to batch PMMA polymerization reactor, Journal of Applied Polymer Science. 69 (1998) 59–68. https://doi.org/10.1002/(SICI)1097-4628(19980705)69:1<59::AID-APP8>3.0.CO;2-L.
[45] A. Singhal, K.A. Dubey, Y.K. Bhardwaj, D. Jain, S. Choudhury, A.K. Tyagi, UV-shielding transparent PMMA/In2O3 nanocomposite films based on In2O3 nanoparticles, RSC Adv. 3 (2013) 20913–20921. https://doi.org/10.1039/C3RA42244E.
[46] C. Ramírez, M. Rico, A. Torres, L. Barral, J. López, B. Montero, Epoxy/POSS organic–inorganic hybrids: ATR-FTIR and DSC studies, European Polymer Journal. 44 (2008) 3035–3045. https://doi.org/10.1016/j.eurpolymj.2008.07.024.
[47] G. He, F. Gong, J. Liu, L. Pan, J. Zhang, S. Liu, Improved mechanical properties of highly explosive-filled polymer composites through graphene nanoplatelets, Polymer Composites. 39 (2018) 3924–3934. https://doi.org/10.1002/pc.24431.
[48] D.G. Papageorgiou, M. Liu, Z. Li, C. Vallés, R.J. Young, I.A. Kinloch, Hybrid poly(ether ether ketone) composites reinforced with a combination of carbon fibres and graphene nanoplatelets, Composites Science and Technology. 175 (2019) 60–68. https://doi.org/10.1016/j.compscitech.2019.03.006.
[49] D. Roylance, Engineering Viscoelasticity, (2001). https://ocw.mit.edu/courses/materials-science-and-engineering/3-11-mechanics-of-materials-fall-1999/modules/MIT3_11F99_visco.pdf.

[50] P. Nising, High-temperature radical polymerization of methyl methacrylate in a continuous pilot scale process, D.Sc., ÉCOLE POLYTECHNIQUE FÉDÉRALE DE LAUSANNE, 2006. https://pdfs.semanticscholar.org/914c/389f24e599cb149a84ab8219392e5a6d5df8.pdf (accessed May 27, 2020).
[51] H. Wang, C. Ma, W. Zhang, H.-M. Cheng, Y. Zeng, Improved Damping and High Strength of Graphene-Coated Nickel Hybrid Foams, ACS Appl. Mater. Interfaces. 11 (2019) 42690–42696. https://doi.org/10.1021/acsami.9b10382.
[52] N. Rajini, J.W. Jappes, S. Rajakarunakaran, P. Jeyaraj, Dynamic mechanical analysis and free vibration behavior in chemical modifications of coconut sheath/nano-clay reinforced hybrid polyester composite:, Journal of Composite Materials. (2012). https://doi.org/10.1177/0021998312462618.
[53] K.F. Graff, Wave Motion in Elastic Solids, Revised edition, Dover Publications, New York, 1991.
[54] L. Gong, I.A. Kinloch, R.J. Young, I. Riaz, R. Jalil, K.S. Novoselov, Interfacial Stress Transfer in a Graphene Monolayer Nanocomposite, Advanced Materials. 22 (2010) 2694–2697. https://doi.org/10.1002/adma.200904264.
[55] R.M. Kully, Dynamic Energy Absorption of Eco-Core and Other Commercial Core Materials, in: B. Song, L. Lamberson, D. Casem, J. Kimberley (Eds.), Dynamic Behavior of Materials, Volume 1, Springer International Publishing, Cham, 2016: pp. 53–60. https://doi.org/10.1007/978-3-319-22452-7_9.
[56] V.S. Deshpande, N.A. Fleck, High strain rate compressive behaviour of aluminium alloy foams, International Journal of Impact Engineering. 24 (2000) 277–298. https://doi.org/10.1016/S0734-743X(99)00153-0.
[57] T. Mukai, T. Miyoshi, S. Nakano, H. Somekawa, K. Higashi, Compressive response of a closed-cell aluminum foam at high strain rate, Scripta Materialia. 54 (2006) 533–537. https://doi.org/10.1016/j.scriptamat.2005.10.062.
[58] M. Peroni, G. Solomos, V. Pizzinato, Impact behaviour testing of aluminium foam, International Journal of Impact Engineering. 53 (2013) 74–83. https://doi.org/10.1016/j.ijimpeng.2012.07.002.
[59] H. Yamada, T. Kami, R. Mori, T. Kudo, M. Okada, Strain Rate Dependence of Material Strength in AA5xxx Series Aluminum Alloys and Evaluation of Their Constitutive Equation, Metals. 8 (2018) 576. https://doi.org/10.3390/met8080576.
[60] S.J. Pérez-Bergquist, G.T. (Rusty) Gray, E.K. Cerreta, C.P. Trujillo, A. Pérez-Bergquist, The dynamic and quasi-static mechanical response of three aluminum armor alloys: 5059, 5083 and 7039, Materials Science and Engineering: A. 528 (2011) 8733–8741. https://doi.org/10.1016/j.msea.2011.08.046.
[61] C.J. Maiden, S.J. Green, Compressive Strain-Rate Tests on Six Selected Materials at Strain Rates From 10−3 to 104 In/In/Sec, J. Appl. Mech. 33 (1966) 496–504. https://doi.org/10.1115/1.3625114.
[62] L. Djapic Oosterkamp, A. Ivankovic, G. Venizelos, High strain rate properties of selected aluminium alloys, Materials Science and Engineering: A. 278 (2000) 225–235. https://doi.org/10.1016/S0921-5093(99)00570-5.
[63] G.H. Majzoobi, S.H.A. Nejad, S.A.R. Sabet, Mechanical characterization of graphene oxide reinforced epoxy at different strain rates, Polymer Engineering & Science. 59 (2019) 1636–1647. https://doi.org/10.1002/pen.25162.
[64] P. Jindal, S. Pande, P. Sharma, V. Mangla, A. Chaudhury, D. Patel, B.P. Singh, R.B. Mathur, M. Goyal, High strain rate behavior of multi-walled carbon nanotubes–polycarbonate composites, Composites Part B: Engineering. 45 (2013) 417–422. https://doi.org/10.1016/j.compositesb.2012.06.018.
[65] N.K. Naik, K.S. Pandya, V.R. Kavala, W. Zhang, N.A. Koratkar, High-strain rate compressive behavior of multi-walled carbon nanotube dispersed thermoset epoxy resin:, Journal of Composite Materials. (2014). https://doi.org/10.1177/0021998314527329.

[66] J. Chen, X. Mao, G. Wang, Mechanical Properties of MWCNTs/PA66 Composites under Impact Loading, DEStech Transactions on Engineering and Technology Research. 0 (2016). https://doi.org/10.12783/dtetr/ameme2016/5776.
[67] R. Panduranga, K. Shivakumar, L. Russell, Energy Absorption Performance of a Eco-Core - A Syntactic Foam, in: 48th AIAA/ASME/ASCE/AHS/ASC Structures, Structural Dynamics, and Materials Conference, American Institute of Aeronautics and Astronautics, n.d. https://doi.org/10.2514/6.2007-2336.
[68] T. Nicholas, Tensile testing of materials at high rates of strain, Experimental Mechanics. 21 (1981) 177–185. https://doi.org/10.1007/BF02326644.
[69] G.H. Staab, A. Gilat, A direct-tension split Hopkinson bar for high strain-rate testing, Experimental Mechanics. 31 (1991) 232–235. https://doi.org/10.1007/BF02326065.
[70] O.S. Lee, M.S. Kim, Dynamic material property characterization by using split Hopkinson pressure bar (SHPB) technique, Nuclear Engineering and Design. 226 (2003) 119–125. https://doi.org/10.1016/S0029-5493(03)00189-4.